Characterization of the interface between an Fe–Cr alloy and the p-type thermoelectric oxide Ca3Co4O9

Holgate, Tim; Han, Li; Wu, NingYu; Bøjesen, Espen Drath; Christensen, Mogens ; Iversen, Bo B.; Van Nong, Ngo; Pryds, Nini

Published in:
Journal of Alloys and Compounds

Link to article, DOI:
10.1016/j.jallcom.2013.08.096

Publication date:
2014

Characterization of the interface between an Fe-Cr alloy and the *p*-type thermoelectric oxide $Ca_3Co_4O_9$

Tim C. Holgate, Li Han, NingYu Wu, Espen D. Bøjesen, Mogens Christensen, Bo B. Iversen, Ngo Van Nong, Nini Pryds

PII: S0925-8388(13)01956-7
DOI: http://dx.doi.org/10.1016/j.jallcom.2013.08.096
Reference: JALCOM 29230

To appear in:

Please cite this article as: T.C. Holgate, L. Han, N. Wu, E.D. Bøjesen, M. Christensen, B.B. Iversen, N.V. Nong, N. Pryds, Characterization of the interface between an Fe-Cr alloy and the *p*-type thermoelectric oxide $Ca_3Co_4O_9$, (2013), doi: http://dx.doi.org/10.1016/j.jallcom.2013.08.096

Characterization of the interface between an Fe-Cr alloy and the *p*-type thermoelectric oxide $Ca_3Co_4O_9$

Tim C. Holgate[1], Li Han[1], NingYu Wu[1], Espen D. Bøjesen[2], Mogens Christensen[2], Bo B. Iversen[2], Ngo Van Nong[1] and Nini Pryds[1]

[1]*Dept. of Energy Conversion and Storage, Technical University of Denmark, Risø Campus, Frederiksborgvej 399, Building 779, 4000 Roskilde, Denmark*

[2]*Centre for Materials Crystallography, Department of Chemistry and iNANO, Aarhus University, 8000 Aarhus C, Denmark*

Abstract

A customized Fe-Cr alloy that has been optimized for high temperature applications in oxidizing atmospheres has been interfaced via spark plasma sintering (SPS) with a p-type thermoelectric oxide material: calcium cobaltate ($Ca_3Co_4O_9$). The properties of the alloy have been analyzed for its compatibility with the $Ca_3Co_4O_9$ in terms of its thermal expansion and transport properties. The thermal and electrical contact resistances have been measured as a function of temperature, and the long term electronic integrity of the interface analyzed by measuring the resistance versus time at an elevated temperature. The kinetics of the interface have been analyzed through imaging with scanning electron microscopy (SEM), elemental analysis using energy dispersive spectroscopy (EDS), and phase identification with X-ray diffraction (XRD). The results reveal the formation of an intermediate phase containing calcium and chromium in the interface that is highly resistive at room temperature, but conducting at the intended thermoelectric device hot-side operating temperature of 800°C. As the alloy is well matched in terms of its thermal expansion and highly conducting compared to the $Ca_3Co_4O_9$, it may be further considered as an interconnect material candidate at least with application on the hot-side of an oxide thermoelectric power generation module.

Introduction

The past several decades have witnessed great advances in materials research pertaining to renewable energy technologies. Oxides often play a role as energy materials in many of these

technologies, such as solid oxide fuel cells (SOFCs) and thermoelectricity. Oxide thermoelectrics are excellent candidates for high temperature thermoelectric (TE) energy conversion due to their chemical stability in air at the high temperatures associated with waste heat recovery (up to 800°C) and the relative low cost and availability of materials[1]. Inevitably, the issue of forming well contacted interfaces (that is to say, exhibiting low thermal and electrical contact resistance) between these oxides and pure metals or alloys serving as interconnects must be addressed in order to minimize the internal resistances of the modules to maximize the power output. This issue is compounded at high temperatures in that the chemical stability of the metal-oxide interface is undermined by mass diffusion and the formation of intermediate phases that may degrade the electrical and structural integrity of the interface. Wide-scale implementation of oxide thermoelectric power generation modules in the recovery of waste heat energy will require the development of oxide TE-interconnect contact interfaces that are long term chemically and electrically stable in air and minimal in their contribution to the internal resistances of modules.

Several reviews have covered the extensive work on contact resistances between metal interconnects and oxide cathode and anode materials in SOFCs[2,3]. While a great deal of information may be gleaned from the work in SOFCs, there are a few key differences between SOFCs and oxide TE applications. First of all, SOFCs involve both oxidizing and reducing atmospheres whereas oxide TEs generally only operate in air. Secondly, the excepted value of area specific contact resistance (ASR) for SOFCs (<100 $m\Omega \cdot cm^2$) is unacceptably high by a few orders of magnitude for oxide TE applications. This is due to their considerably lower densities (SOFC cathodes and anodes are porous) and higher intrinsic resistivities than oxide TE materials. So while the issue of atmosphere is simpler for oxide TEs, the issue of the contact resistance of metal interconnect-oxide TE interfaces may be more demanding to solve since it is the relative

magnitude of the contact resistance in comparison to the intrinsic material resistances that matters.

There have been a limited number of works that address the issue of contact resistance in both alloy/intermetallic[4,5,6] and oxide thermoelectric devices[7,8,9,10,11]. As for the latter, $Ca_3Co_4O_9$ (pure or doped) was used as the *p*-type material in all but ref. 11 (Arai et al.) which used a related cobaltate—$NaCo_2O_4$. Several other well-known studies have focused on $Ca_3Co_4O_9$ as the *p*-type TE element of a unicouple or TE module but without quantitative analysis of the contact resistances[12,13,14,15]. In these studies, the authors made contact between TE elements using either screen printed Ag paste[14,15] or combination of Ag paste mixed with a few percent of oxide TE powders and Ag foil[12,13], with the latter resulting in a decrease of the total internal resistance and better stability of the $Ca_3Co_4O_9$ based TE modules.

As for refs. 7-10, the contact resistance was obtained by subtracting the theoretical resistances of the TE elements based on their intrinsic resistivities and dimensions from the total measured resistances of the unicouples or modules; only Arai et al.[11] used a preferred method of extrapolating a resistance versus distance to the interface to quantify the contact resistance. In their work, Arai et el. successfully formed stable contacts between Ni interconnects and both *p*-type $NaCo_2O_4$ and *n*-type Mg_2Si via spark plasma sintering (a method also used by Zhao et al.[5]) by introducing a buffer layer of Ni powder mixed with $SrRuO_3$ between the Ni interconnect and the TE elements—presumably inhibiting the growth of NiO at the interface.

The work presented herein explores the feasibility of a high performance Fe-Cr alloy as an interconnect material in oxide thermoelectric power generation modules where the p-type TE element is calcium cobaltate. Using SPS as the method for interfacing and a careful measurement

of the contact resistance by extrapolation of the resistance versus distance to the interface, the analysis of an Fe-Cr alloy is presented and discussed both in terms of the magnitude of the contact resistance and the long term stability of the interface at high temperatures. A tailored Fe-22%Cr alloy (denoted as Fe22Cr) was chosen for this study in light of the success of high-chrome steel alloys in high temperature solid oxide fuel cell applications—mainly due to their high temperature corrosion resistance and a thermal expansion coefficient on the order of many conducting oxides[2].

II. Experimental Methods

2.1 Sample Preparation

The interfaces were formed by first pelletizing the alloy powders (average particle size of ~47μm) using a spark plasma sintering (SPS) system (Dr. Sinter 515S, Fuji Electronic Industrial Co., Japan). The pellet was then cut and polished with P1000 SiC metallurgical paper, placed back into the graphite SPS dies, and the $Ca_3Co_4O_9$ powders placed on top of the alloy pellet (Fig. 1). The densification of the $Ca_3Co_4O_9$ and the formation of the interface were then performed simultaneously at conditions optimized for the $Ca_3Co_4O_9$[16]. Forming the interface directly using SPS was decided upon because of the mechanical strength and scalability that the process may provide. Though the high current density involved in the highly dynamic SPS process may result in an expedited initial growth of interfacial secondary phases, the eventual formation of these phases at operational temperatures mitigates this possible disadvantage of the SPS process.

Both bi-layered (Fe22Cr/$Ca_3Co_4O_9$) and tri-layered ($Ca_3Co_4O_9$/Fe22Cr/$Ca_3Co_4O_9$) samples were prepared for the various characterization measurements (Fig. 1). Additionally, a comparative sample of pure nickel with $Ca_3Co_4O_9$ was prepared in the same manner using 400 mesh (< 47

μm) Ni powders (Alfa Aesar, 99.99%). Samples were cut with a diamond saw, polished with SiC metallurgical paper and cleaned with ethanol before measurements. Additionally, pure samples of both Fe22Cr and $Ca_3Co_4O_9$ were prepared for individual characterization in order to determine their contributions to the properties of the layered samples. The density of the Fe22Cr sample measured using Archimedes' method was 7.67 g/cm^3. Using a statistical pixel counting method performed on cross-sectional scanning electron micrograph digital images, the Fe22Cr sample exhibited a porosity of about 1.1%, which corresponds to a full density of 7.76 g/cm^3—a value that agrees well with the theoretical density calculated using lattice parameters determined by X-ray diffraction (Bruker D8, Cu-k_α): 7.78 g/cm^3. In all cases, the densities of the $Ca_3Co_4O_9$ samples were more than 99% of the theoretical density (4.68 g/cm^3)[17] and showed no porosity.

2.2 Transport Measurement Methods

The thermal and electronic transport across the interfaces were measured using a Netzch LFA-457 laser flash apparatus and a custom built system utilizing the four-probe technique, respectively. Specifically, the thermal contact resistance was determined by first measuring the thermal diffusivity of Fe22Cr and $Ca_3Co_4O_9$ independently using the Cape-Lehman model[18]. Data were measured on the bi-layered samples and the single layer results fed back into the Netzsch LFA analysis software using a model for two-layers with contact resistance (based on the work of Hartmann et al.[19]).

The initial electrical contact resistance after interfacing via SPS was measured on bar-shaped bi-layered samples from room temperature up to 800°C. The schematic of the custom system used is presented in Fig. 2. This configuration allows for the determination of the resistivity of each component material, as well as the contact resistance (R_c) of the interface by linear extrapolation

of the resistance (R) versus the distance to the interface ($x_{n\ to\ 0}$) and subsequent subtraction of the contribution from the alloy between the probe lead and the interface:

$$R_C = intercept(R\ vs.\ x_{6...3\ to\ 0}) - R_{1\ to\ 3}\frac{x_{1\ to\ 3}}{x_{2\ to\ 0}} \quad \text{(Eq. 1)}$$

Using a four-probe Keithley 580 Micro-ohmmeter and a double-pole, 6-throw rotary switch, the current was injected at the two ends of the sample and the voltage probed at various positions along the surface and across the interface via 0.1mm platinum wire leads affixed with silver paste. The separation of the leads and positions relative to the interface were measured using the *cell-A* software package with images taken from an Olympus SC20 digital camera affixed to an Olympus SZX9 stereomicroscope. The voltage leads were arranged so that the four leads used to obtain the resistance as a function of distance to the interface data were evenly spaced along the $Ca_3Co_4O_9$. The order of magnitude higher resistivity of the TE oxide compared to the interconnect allowed for a high signal-to-noise ratio in the four-probe measurement of the Keithley micro-ohmmeter and easy subtraction of the contribution of the interconnect to the intercept of $R\ vs.\ x_{N\ to\ 0}$.

The Keithley micro-ohmmeter was set to pulse mode where the current is imputed and the voltage probed for 150 milliseconds and then the current is shutoff and a baseline voltage obtained for subtraction. This baseline voltage should account for any offsets due to thermal gradients, i.e., thermoelectric voltages. Still, measurements were taken with both the forward and reverse current configurations and the results averaged. Data was not recorded for a given temperature until both the system temperature was stabilized and the difference in forward and reverse mode resistances minimized.

In both measurements, the "contact" resistance is actually the *interface* resistance, which includes the electrical or thermal resistance of the intermediate phases and their respective contact resistances with the alloy and $Ca_3Co_4O_9$. These resistances are multiplied by the cross-sectional area of the interface to give the area specific resistance of the interface (ASR).

2.3 Microstructures and Interface Evolution

In order to ascertain the chemical stability of the interface, scanning electron microscopy (SEM) was employed with energy dispersive x-ray spectroscopy (EDS). As-prepared interfaced samples were cross-sectioned and polished for imaging and compositional analysis. Samples that underwent high temperature cycling during measurements or long term annealing at high temperatures (generally 800°C, which is the intended module hot-side temperature) were likewise prepared in order to observe the microstructural and compositional evolution of the interfaces. Imaging and analysis were performed using a Zeiss Supra-35 equipped with a Noran EDS system. Powder diffraction patterns were collected near the-oxide metal interface using a Rigaku Smartlab diffractometer equipped with a Cu-Kα rotating anode and parallel beam selection from the cross beam optics unit. A constant incidence angle of 23° was used together with a 0.04 mm slit opening resulting in a beam foot print of approximately 100 μm. Powder patterns were collected using a D/teX Ultra detector operated in florescence suppression mode. The sample position was moved by 50 μm between each data collection.

Additionally, the time evolution of the resistance across the interface was assessed using a custom built apparatus that is described elsewhere[20]. Using a pseudo-four-probe resistance measurement technique, the total resistances of tri-layered pellets, each consisting of a thin disk of interconnect material (i.e. Ni400—spark plasma sintered 400 mesh Ni powder[20]—and

Fe22Cr) sandwiched between two $Ca_3Co_4O_9$ layers, were measured as a function of time. One of the four independent channels of the apparatus was reserved for the simultaneous measurement of a $Ca_3Co_4O_9$ pellet lacking an interface to detect and account for any changes in the resistance not originating at an interconnect-TE oxide interface (e.g. the interface of the platinum wire mesh probe leads and the $Ca_3Co_4O_9$ as well as the $Ca_3Co_4O_9$ intrinsically). Expressed in terms of a change in resistance normalized to the some initial resistance, this data and the derivatives with respect to temperature may give indication as to whether the diffusion/reaction processes they arise from will be time-limited and on what time scale.

2.4 Material Properties Characterization

As it was necessary to characterize the custom alloy and oxide TE materials in order to better interpret the data of the interfaced samples, the thermal expansion and electrical resistivity as functions of temperature were measured on Fe22Cr and a representative sample of $Ca_3Co_4O_9$ using a Netzsch DIL 402 C dilatometer and an Ulvac ZEM3 resistivity and thermopower measurement system, respectively. The thermal conductivity (κ) was calculated with Eq. 2 using the thermal diffusivity (D) and specific heat capacity (c_p), both measured by the laser flash method (Netzsch LFA-457), and the density (d) measured by Archimedes' method.

$$\kappa = d \cdot D \cdot c_p \qquad \text{(Eq. 2)}$$

III. Results and Discussion

3.1 Material Properties

Interfacial strains at the interface inevitably result from a mismatch in the thermal expansion coefficients (α_T) of the two materials involved at high temperature operation. As noted in the introduction, Fe22Cr was designed to have a thermal expansion coefficient sufficiently close to that of oxides commonly used in solid oxide fuel cell applications. To verify the compatibility of the alloy to the TE material $Ca_3Co_4O_9$, the thermal expansion was measured between room temperature and 800 – 850°C for both Fe22Cr and $Ca_3Co_4O_9$. Because the latter is known to exhibit anisotropic properties, the sample was measured perpendicular (in-plane) to the direction of applied SPS pressure as well as parallel (out-of-plane).

The technical thermal expansion coefficients ($^{\Delta L}/_{[L_o \Delta T]}$) of Fe22Cr and $Ca_3Co_4O_9$ are presented in Fig. 3 with the differential α_T ($^{\partial L}/_{[L_o \partial T]}$) of $Ca_3Co_4O_9$ displayed in the inset. It is important to note that the in-plane α_T of the Co349 is more relevant because this direction is perpendicular to the interface formed by SPS in multilayer pellets. Therefore, it is the relative thermal expansion between materials along this direction that will most influence the strains at the interface. As expected, the thermal expansion of Fe22Cr is well matched to that of $Ca_3Co_4O_9$—both being between 10 and 12 x $10^{-6}K^{-1}$ and no more than ~5% difference over the whole temperature range. Confidence in these results is given by the close agreement with literature values of conventionally sintered $Ca_3Co_4O_9$ samples reported by Cheng et al.[21] and Kenfaui et al.[22] (10 – 13 x $10^{-6}K^{-1}$ and 12.6 x $10^{-6}K^{-1}$, respectively). These values, which fall in between those of the "*a*-*b*" and "*c*" directions of highly aligned samples, suggest only a small degree of texturing.

The inset of Fig. 3 shows the derivative of $\Delta L/L_o$ with respect to the temperature for both the in-plan and out-of-plane samples of $Ca_3Co_4O_9$. The sharp step in the α_T of $Ca_3Co_4O_9$ near 300°C may be due to a first-order metal-semiconductor transition. However, while this type of transition in $Ca_3Co_4O_9$ has been observed by others, it is expected around 123°C[21]. Although interesting, this discrepancy is out of the scope of this work and will be investigated in the future. As for this study, it is only important to note that the thermal expansions of the alloys are well matched to the $Ca_3Co_4O_9$.

In the α_T curve of Fe22Cr, two second order transitions at about 500°C and just beyond 600°C can be observed. These transitions are also manifested in the resistivity curve, although there they are less pronounced (Fig. 4). The boundary of the miscibility gap where the binary alloy Fe-22%Cr separates into Fe- and Cr-rich alpha phases is located between 500 – 510°C[23]. At 22% Cr, the BCC Fe-Cr solid solution alpha phase coexists with a lower symmetry, slightly Fe-rich sigma phase above this eutectoid boundary up to the vicinity of 600 – 650°C where the system becomes totally miscible[23].

The thermal conductivity (Fig. 4) exhibits first a drop after 500°C due to the precipitation of the sigma phase, but then a sharp increase above 600°C due to the homogenization of the crystal structure into the Fe-rich alpha phase. Of course the dwell time at each temperature before the measurement of the thermal diffusivity (used to obtain conductivity) is likely not long enough to obtain a steady state, but the exact value of the thermal conductivity is not relevant to the results

of this study and it is only important to note that the magnitude is nearly an order higher than that of $Ca_3Co_4O_9$[16]. Additionally, the dilute amounts of the many other metallic elemental components of the Fe22Cr alloy used in this study undoubtedly complicate the phase mapping of the systems, but the Fe-Cr binary system may still serve as a guide in understanding the observed trends in the thermal expansion and transport data.

The electrical transport properties of Fe22Cr are typical of a metallic alloy with a low thermopower (less than 16μV/K over the whole temperature range) and an electrical resistivity that is metallic in nature—increasing with temperature and exhibiting low values on the order of 50 – 120 μΩ·cm.

3.2 Interface Composition and Evolution

As previously reported on Ni/ $Ca_3Co_4O_9$[20], the direct interfacing of Fe22Cr with $Ca_3Co_4O_9$ via SPS resulted in the initial formation of an intermediate phase. EDS line and spot analysis (Figure 5b, Table 2) of the interface suggests that the intermediate phase of the Fe22Cr/ $Ca_3Co_4O_9$ interface may be calcium chromate ($CaCrO_4$) or possibly the perovskite $CaCrO_3$. The interface resistance discussed later suggests the insulating[24] calcium chromate as the latter is a metallic oxide[25]. The stepwise XRD "line" scans presented in inset of Figure 5c clearly display the transition from pure calcium cobaltate to the iron-chrome alloy with the intermediate phases at the interface. In the main panel of 5c is the scan taken at the interface, which contain the most dominant peaks of the $CaCrO_4$ phase at 2θ = 24.9°, 33.4° and 49.2°. However, there are no observable peaks where only the $CaCrO_3$ phase should appear—most notably none at 33.9° where it's dominant peak ought to be. Also, detected by the EDS line scan in Figure 5b is a thin layer of chromium oxide, however its presence is not clearly discernable by the XRD step scans

due to its small volume fraction and the proximity of its main peaks to other prominent peaks of the main phases. However, cobalt oxide (Co_3O_4) was detected by its dominant peak at about 36.9° and EDS mapping (not shown) indicates this to be some of the small particles that make up the islands within the $CaCrO_4$ phase as well in the $Ca_3Co_4O_9$ bulk near the interface.

The time evolution of the Fe22Cr/ $Ca_3Co_4O_9$ interface from zero (as SPS'ed) to 360 hours at 800°C in air is presented in Fig. 5a. Compared to the intermediate $Ni_{1-x}Co_xO$ phase of the Ni/ $Ca_3Co_4O_9$ sample of Ref. 20, which grew to about 20 μm after 300 hours, the kinetics of the intermediate phase of the Fe22Cr/ $Ca_3Co_4O_9$ sample is slower, growing only to about 12 ± 2 μm after 360 hours at the same conditions (Table 1). The slower growth of the intermediate $CaCrO_4$ phase may be a result of the thinner layer of the stable chromium oxide (quantization of the EDS results suggests Cr_2O_3) that is formed at the surface of the alloy. In comparison, the NiO layer formed at the surface of the Ni in Ni/ $Ca_3Co_4O_9$ interfaces facilitates a high self-diffusivity of Ni[26] which feeds its intermediate layer. Understanding the mass diffusion kinetics within the $CaCrO_4$ layer may be helpful in order to mitigate its growth. Presumably, the Cr diffusion in the Fe-Cr alloy will control the formation and growth of the Cr_2O_3 phase, which feeds the $CaCrO_4$ growth. While it is uncertain whether it is the Cr or Ca that is mobile in the intermediate phase, the preservation of cobaltate ($Ca_3Co_4O_9$ and/or $Ca_2Co_2O_5$) islands in the growing intermediate phase (Fig. 5) suggests that it is the former of the two. Indeed, the concept of Cr "poisoning" of alkali and alkaline earth containing metal oxides is a well known phenomenon within the solid oxide fuel cell community[27].

3.3 Electrical Contact

Bi-layered bar shaped samples of nickel and Fe22Cr interfaced with $Ca_3Co_4O_9$ were prepared and the electrical resistivity measured from room temperature to 800°C in air. However, the nickel sample delaminated after 600°C due to the mismatch in thermal expansion between Ni and $Ca_3Co_4O_9$. In the case of Fe22Cr the intermediate $CaCrO_4$ layer formed during the SPS processing was too resistive below 300°C to get a meaningful result by extrapolation, and so the total resistance measured between lead positions 2 and 3 (just on either side of the interface) was taken to be the interfacial contact resistance. The forward and reverse current resistivities of a sample point (Fe22Cr, 600°C) can be found in the inset of Fig. 6. The small difference in the forward and reverse current data may be from a Schottky-like barrier due to a difference in electronic band structure between the intermediate $CaCrO_4$ phase and either the interconnect or the $Ca_3Co_4O_9$. However, without access to the raw V(I) data of the micro-ohmmeter it is impossible to know the quality of the subtraction and calculation of the resistances by the Keithley 580. A simple V-I plot of data measured across the interface between a single pair of leads may assist in assessing the source of the discrepancies between forward and reverse current resistances, and such experiments are planned for the future. However, the differences between the intercepts of the data taken in forward and reverse current modes are acceptably small enough to justify averaging the calculated contact resistances.

In the main panel of Fig. 6 the natural logarithms of the area specific contact resistances (ASR_C) of these samples as a function of inverse temperature are presented. The interfacial resistance of all samples exhibited a change in their temperature dependences near 300°C, corresponding to the first-order transition of $Ca_3Co_4O_9$[17]. For Ni400/ $Ca_3Co_4O_9$, there is also an obvious step in the

data, dropping above the transition temperature presumably because the interfacial strain should be less at higher temperatures due to the fact that the samples were interfaced in the SPS system at 850°C. To test the repeatability of the data a second Fe22Cr/ $Ca_3Co_4O_9$ sample was produced using an entirely different batch of $Ca_3Co_4O_9$ powders and the two data sets of each sample are in agreement within about 10%.

Due to the ionic nature of the $CaCrO_4$ intermediate layer, the contact resistance of the Fe22Cr/ $Ca_3Co_4O_9$ interface is very high—on the order of a few to a few hundred Ω-cm^2 between room temperature and just above 200°C. The interfacial contact resistance quickly drops with increasing temperature, but the dependence of the natural logarithm of ASR_C on the inverse of temperature is not quite linear as would be expected for thermally activated hopping conduction in the intermediate layer of the interface. This unexpected result may be from a low density of data in which several regions of linear dependence may reside between locations of transitions in either the $Ca_3Co_4O_9$ or the Fe-Cr alloys, which may result in nonlinear changes in interfacial strain. Again, the measured ASR_C includes contributions from the intrinsic resistivity of the intermediate layer or layers as well as the actual contact resistances between each phase due to their inherent differences in band structure and the planar defects associated with interfaces of any kind. The highest temperature results of this data are presented in Table 2a for comparison.

The high temperature (~800°C) change in resistance versus time of tri-layered samples that was investigated in order to assess the long term integrity of the interfaces in terms of electronic conduction is presented in Fig. 7 along with an inset displaying their derivatives with respect to time. The changes in the resistances of the samples are relative to and normalized by the values

at 60 hours. This value was chosen in order to exclude the initial transient portion of the data and compare only the data where the kinetics are in something more of a steady state.

The results of this test reveal the interface of Fe22Cr with $Ca_3Co_4O_9$ to be more stable than the Ni/ $Ca_3Co_4O_9$ interface, and combined with a comparison of the micrographs of Fig. 5a with the results of Ni with $Ca_3Co_4O_9$ reported in Ref. 20, the reason is the slower growth rate of the $CaCrO_4$ intermediate phase in Fe22Cr/Co349 compared to the nickel oxide intermediate in the Ni/Co349 system. As care was taken to make geometrically well defined samples for this measurement, a calculation of the contact resistance was performed by the subtraction of the Fe22Cr and $Ca_3Co_4O_9$ contributions to the measured resistance after being corrected by subtracting the offset resistances of the measurement leads determined beforehand. The contact resistances calculated at 60 and 360 hours are displayed in Table 2b for comparison to the results of the more accurate linear extrapolation method.

3.4 Thermal Contact

Evaluation of the area specific thermal contact resistance was performed on a bi-layered pellet similar to the ones prepared for electrical contact resistance measurements shown in Fig. 1, but the thicknesses of the interconnect and $Ca_3Co_4O_9$ layers were both about 1 – 2 mm thick. Also, the sample was measured uncut as a 12.7 mm diameter pellet. While the independently measured raw laser flash data of the interconnect materials and $Ca_3Co_4O_9$ were easily fitted to obtain the diffusivity, the bi-layered samples proved a bit more difficult to accurately fit. The main difficulty came in fitting the tail of the data several half-times beyond the maximum. For this reason, the fitting range of the data was lessened until the data before the maximum was best fit, but never less than 4 half-times, and while the uncertainty of the data is explicitly determined,

the fitting process should be taken into consideration. Nevertheless, the order of magnitude and the general temperature trends are believed to be accurate.

The thermal contact resistances of $Ca_3Co_4O_9$ interfaced with Ni400 and Fe22Cr are presented in Fig. 8. Firstly, it should be noted that the values for Fe22Cr with $Ca_3Co_4O_9$ are two orders of magnitude lower than those of Ni400 with $Ca_3Co_4O_9$. This is likely due to the smaller width of the intermediate $CaCrO_4$ layer formed during interfacing with SPS compared to the NiO of the latter. While the temperature dependence of the thermal contact resistance of the Fe22Cr/ $Ca_3Co_4O_9$ interface exhibits approximately the same temperature dependence as its electrical contact resistances, the thermal contact resistance of the Ni400/ $Ca_3Co_4O_9$ interface has an upward trend with temperature in contrast to its electrical contact resistance. While the temperature dependence of its thermal contact resistance is not well understood, it is likely that the mismatch in thermal expansions and subsequent interfacial strains may play a role.

IV. Conclusions

The Fe-22%Cr based alloy studied in this work is well matched in thermal expansion to the well performing thermoelectric oxide material $Ca_3Co_4O_9$. The electrical contact between these alloys and $Ca_3Co_4O_9$ is compromised by the formation of a $CaCrO_4$ layer in the interface, which is prohibitively resistive below ~500°C. However, 800°C is a likely hot-side operating temperature for the oxide thermoelectric power generation modules for which this interconnect-TE oxide interface is intended and so the possibility of using Fe-22%Cr alloys as an interconnect on the hot-side only is a viable one. At this temperature both the electrical and thermal contact

resistances of the Fe22Cr/ $Ca_3Co_4O_9$ interface are orders of magnitude lower than those of the Ni400/ $Ca_3Co_4O_9$ interface. Additionally, the chemical reaction and diffusion kinetics are slower, resulting in a slower growth rate of the detrimental $CaCrO_4$ phase than the NiO phases of the Ni400/ $Ca_3Co_4O_9$ interface.

Due to the greatly different temperatures of the hot and cold-sides of a high temperature oxide thermoelectric generator, the two sides should be engineered independently with the exception of considering the different thermal expansions in minimizing strains throughout the module as a whole. This could mean that the hot and cold-side interconnect materials and the processes for interfacing them to the TE elements could be completely different. The diffusion and chemical activity of the interface between Fe22Cr and $Ca_3Co_4O_9$ may possibly be minimized, or at least found to be time limited on a reasonable time scale, by either the further engineering of the alloy, the optimization of the SPS interfacing process, and/or the intentional insertion of a conducting oxide buffer layer. Therefore, these materials may be a viable choice to serve as hot-side interconnects.

V. Acknowledgements

The authors would like to thank Karsten Agersted and Pernille Hedemark Nielsen for their assistance with dilatometry measurements as well as Nikolaos Bonanos and Sebastian Molin for some very useful conversations concerning the transport measurements. The authors would also like to thank the Programme Commission on Energy and Environment (EnMi), which is part of the Danish Council for Strategic Research (Contract No. 10-093971), for sponsoring the research of the OTE-POWER project, and the Danish National Research Foundation (DNRF93) for additional funding.

Figures

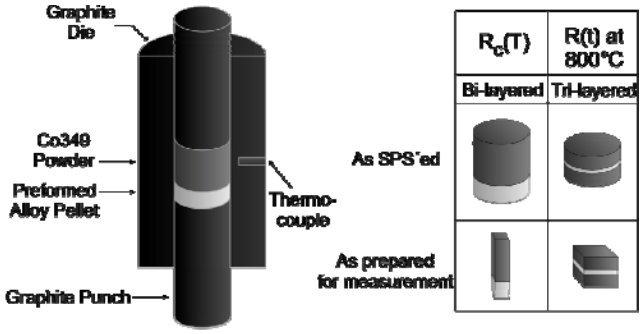

Figure 1. Cross-sectional schematic of the SPS die with punch and sample configuration for simultaneous densification and interfacing of samples.

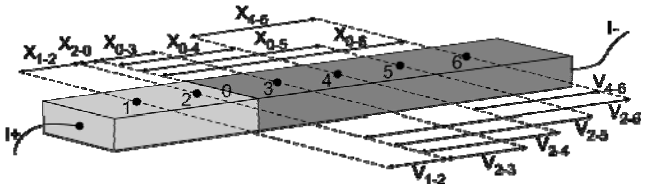

Figure 2. Schematic of the electrical contact resistance measurement configuration. The darker shaded material is the $Ca_3Co_4O_9$ and the sign convention of the current is for forward current mode.

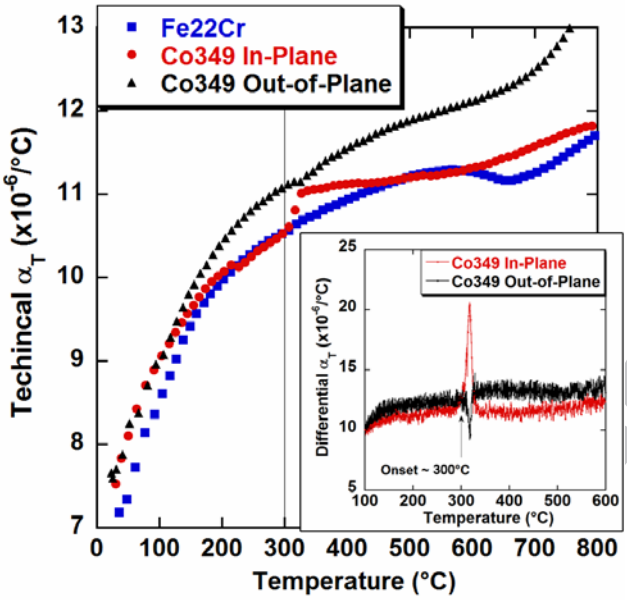

Figure 3. Technical ($\Delta L/[L_o \Delta T]$) thermal expansion coefficients of Fe22Cr and $Ca_3Co_4O_9$ (Co349) from the warming curves. Inset: differential thermal expansion ($\partial L/[L_o \partial T]$) of $Ca_3Co_4O_9$.

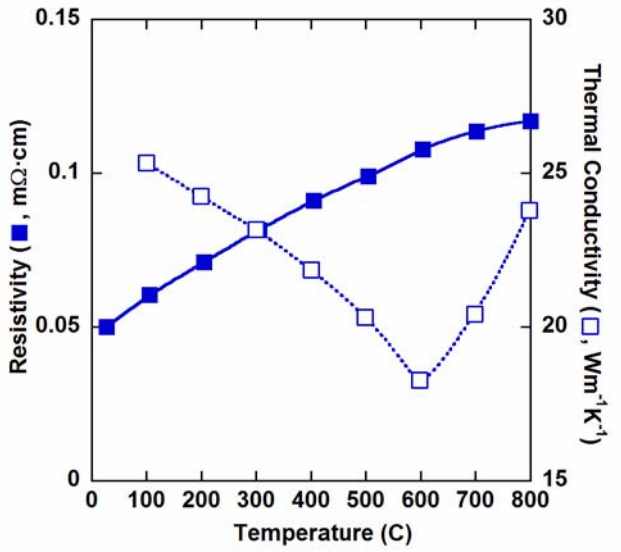

Figure 4. Resistivity and total thermal conductivity of Fe22Cr. The structural transitions exhibited in the thermal expansion data of Fig. 3 affect the thermal conductivity more so than the electrical resistivity.

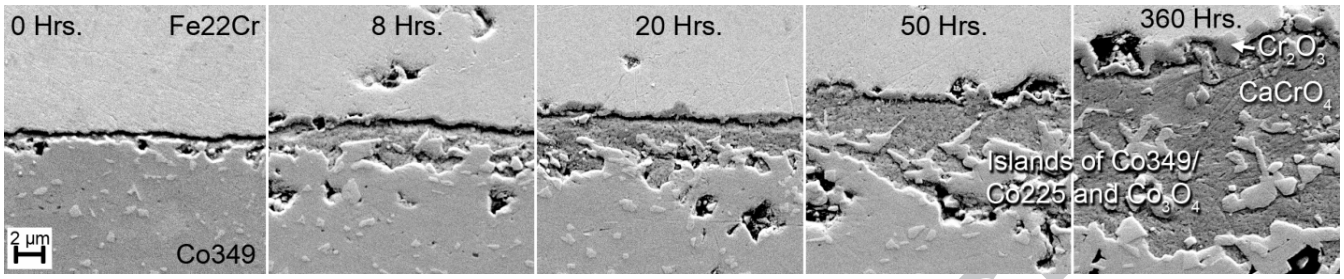

Figure 5a. SEM micrographs of Fe22Cr/$Ca_3Co_4O_9$ samples heat treated for various lengths of time at 800°C in air. These samples were all cut from the same tri-layered pellet from which the resistance vs. time sample was taken. $Ca_3Co_4O_9$ and $Ca_3Co_4O_9$ are denoted by Co349 and Co225, respectively.

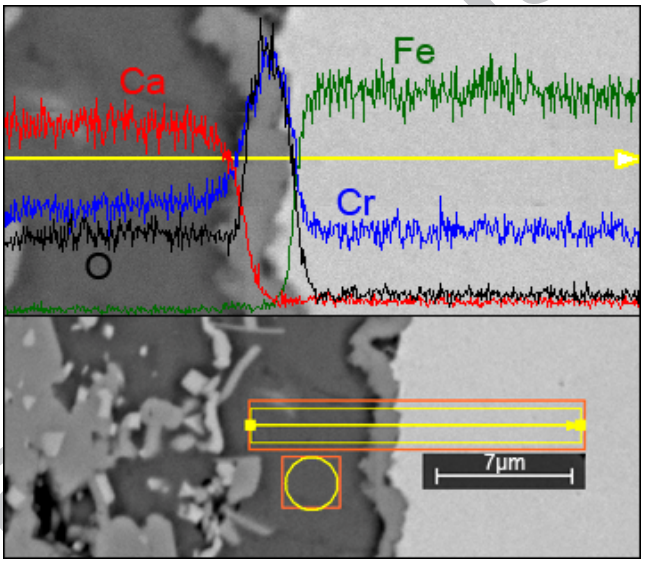

Figure 5b. EDS line scan across the interface between Fe22Cr and the intermediate later after 360 hours. The image is rotated 90° counter-clockwise relative to those of 5a. "Spot" analysis was also performed by analysis of the area enclosed in the circle positioned in the middle of the $CaCrO_4$ layer.

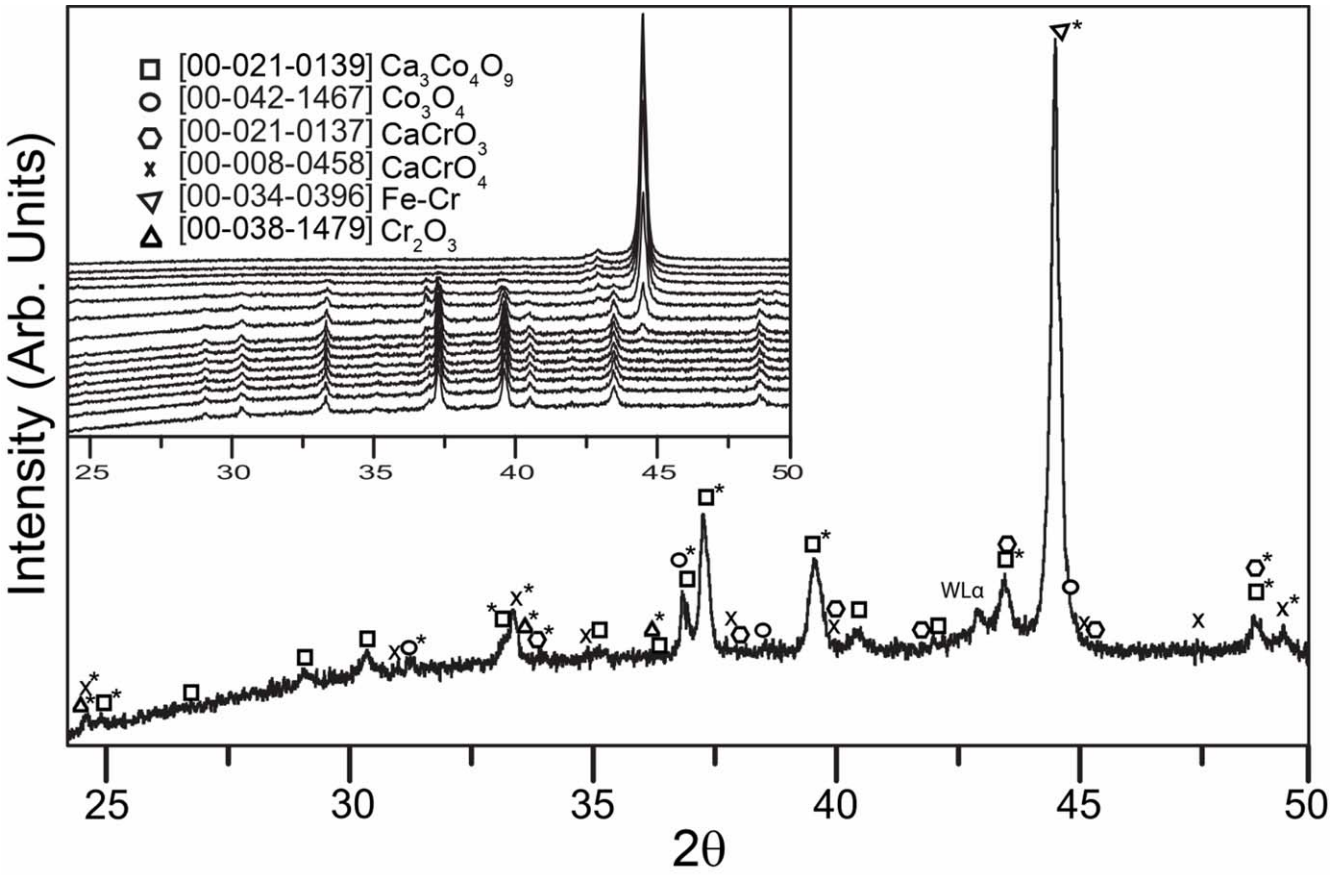

Figure 5c. XRD pattern of the interface with step scan waterfall plot (inset) from the calcium cobaltate (lower) to Fe22Cr. The strongest peaks of the $CaCrO_4$ phase are visible at $2\theta = 24.9°$, 33.4° and 49.2°. The square markers indicate the peaks of the $Ca_3Co_4O_9$ phase, which has the nearly the same diffraction pattern as the $Ca_2Co_2O_5$ phase [00-037-0668] with a very minor additional peak near 36.3°. There is no peak observed near what would be the position of the dominant reflection of the $CaCrO_3$ phase at 33.9°.

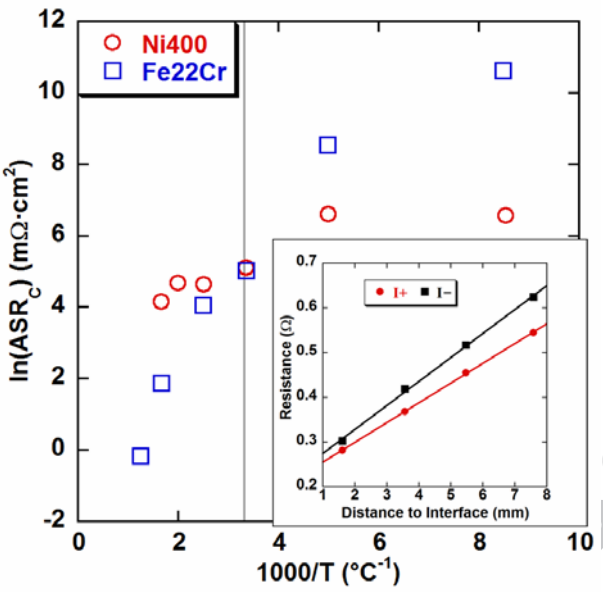

Figure 6. Contact resistance of Ni400 and Fe22Cr with $Ca_3Co_4O_9$ as determined by linear extrapolation of the resistance across the interface of a bi-layered pellet. The vertical line is set at 300°C—near the first-order transition of $Ca_3Co_4O_9$. The inset displays an example (Fe22Cr/$Ca_3Co_4O_9$ at 600°C) of the resistance versus the distance to the interface for both forward and reverse current.

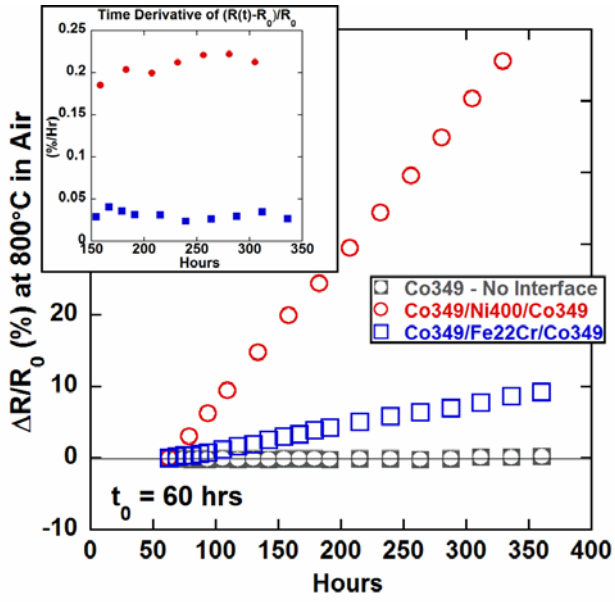

Figure 7. The resistance vs. time of tri-layered pellets in percent change from the values at t = 60 hrs.

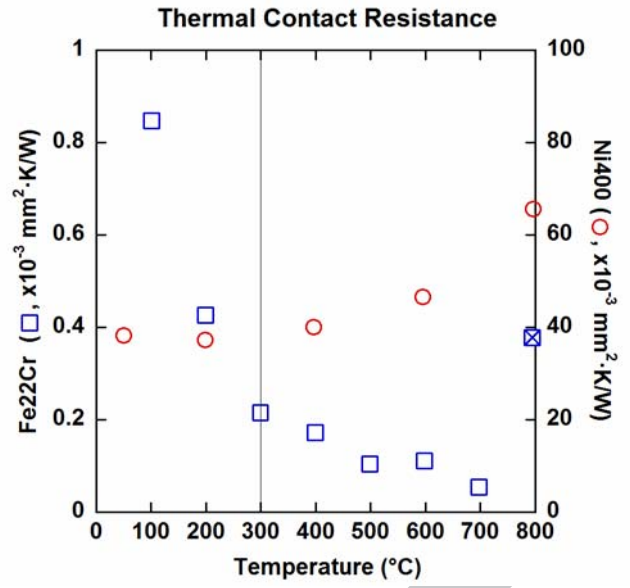

Figure 8. Thermal contact resistances of the Fe22Cr/$Ca_3Co_4O_9$ (squares) and Ni400/$Ca_3Co_4O_9$ (circles) interfaces as a function of temperature. The highest temperature data point of Fe22Cr contains a high degree of uncertainty due to a poor fit of the diffusivity data.

Tables

Hours	$CaCrO_4$ (µm)	Std Dev.	Cr_2O_3 (µm)	+/-
0	0.36	0.13	0.15	0.05
8	1.33	0.58	0.3	0.1
20	1.87	0.37	0.5	0.2
50	3.61	0.97	0.65	0.2
360	12.00	1.82	1.1	0.3

Table 1. Thickness of the main intermediate layer phases as a function of time for Fe22Cr/$Ca_3Co_4O_9$ at 800°C in air.

	wt. %	at. %
Oxygen	40.37	66.07
Chromium	31.92	16.07
Calcium	26.44	17.28
Cobalt	0.66	0.29
Iron	0.60	0.28

Table 2. EDS "spot" analysis results of the intermediate phase.

	Temp (°C)	ASR_C (mΩ·cm2)
Ni400	599.2	63.5
Fe22Cr	800.0	0.84

Table 3a. Initial area specific contact resistance of samples determined by a multi-lead four-probe linear extrapolation to the interface.

T=788°C	ASR_C (mΩ-cm^2)	
	60 Hrs	**360 Hrs**
Fe22Cr	2.0	9.5

Table 3b. Area specific contact resistance after 60 and 360 hours at 788°C obtained from the subtraction of constituent phase contributions from the resistance versus time data.

[1] R. Funahashi, I. Matsubara, H. Ikuta and T. Takeuchi, *Jpn. J. Appl. Phys.* **39** (2000) L1127-L1129.
[2] N. Shaigan, W. Qu, D.G. Ivey and W. Chen, *J. Power Sources* **195** (2010) 1529–1542.
[3] W.Z. Zhu and S.C. Deevi, *Mater. Res. Bull.* **38** (2003) 957–972.
[4] N.A. Matchanov, M. Farhan, J. D'Angelo, E.J. Timm, T.P. Hogan, H. Schock, E.D. Case and M.G. Kanatzidis, *Appl. Sol. Energy* **47** (2011) 90–97.
[5] D. Zhao, H. Geng and L. Chen, *Int. J. Appl. Ceram. Technol.* **9** (2012) 733–741.
[6] J. García-Cañadas, A.V. Powell, A. Kaltzoglou, P. Vaqueiro and G. Min, *J. Electron. Mater.* 42 (2013) 1369–1374.
[7] I. Matsubara, R. Funahashi, T. Takeuchi, S. Sodeoka, T. Shimizu and K. Ueno, *Appl. Phys. Lett.* **78** (2001) 3627–3629.
[8] R. Funahashi, S. Urata, K. Mizuno, T. Kouuchi and M. Mikami, *Appl. Phys. Lett.* **85** (2004) 1036–1038.
[9] E.Sudhakar Reddy, J.G. Noudem, S. Herbert and C. Goupil, *J. Phys. D: Appl. Phys.* **38** (2005) 3751–3755.
[10] L. Han, Y. Jiang, S. Li, H. Su, X. Lan, K. Qin, T. Han, H. Zhong, L. Chen and D. Yu, *J. Alloys Compd.* **509** (2011) 8970–8977.
[11] K. Arai, M. Matsubara, Y. Sawada, T. Sakamoto, T. Kineri, Y. Kogo, T. Iida and K. Nishio, *J. Electron. Mater.* 41 (2012) 1771–1777.
[12] S. Urata, R. Funahashi, R. Mihara, A. Kosuga, S. Sodeoka and T. Tanaka, *Int. J. Appl. Ceram. Technol.* **4** (2007) 535–540.
[13] R. Funahashi and S. Urata, *Int. J. Appl. Ceram. Technol.* **4** (2007) 297–307.
[14] S.M. Choi, K.H. Lee, C.H. Lim and W.S. Seo, *Energy Convers. Manage.* **52** (2011) 335–339.
[15] C.H. Lim, S.M. Choi, W.S. Seo and H.H. Park, *J. Electron. Mater.* **41** (2012) 1247–1255.
[16] N. Wu, T.C. Holgate, N.V. Nong, N. Pryds and S. Linderoth, *J. Electron. Mater.* 42 (2013) 2134–2142.
[17] A.C. Masset, C. Michel, A. Maignan, M. Hervieu, O. Toulemonde, F. Studer, B. Raveau, J. Hejtmanek, *Phys. Rev. B.* **62** (2000) 166–175.
[18] J.A. Cape and G.W. Lehman, *J. Appl. Phys.* **34** (1963) 1909–1913.
[19] J. Hartmann, O. Nilsson and J. Fricke, *High Temp.-High Press.* **25** (1993) 403.
[20] T.C. Holgate, N. Wu, M. Søndergaard, B. Iversen, N.V. Nong, N. Pryds, *J. Electron. Mater.* 42 (2013) 1661–1668.
[21] J. Cheng, Y. Sui, Y. Wang, X. Wang and W. Su, *Appl. Phys. A* **94** (2009) 911–916.
[22] D. Kenfaui, G. Bonnefont, D. Chateigner, G. Fantozzi, M. Gomina and J.G. Noudem, *Mat. Res. Bull.* **45** (2010) 1240–1249.
[23] W. Xiong, M. Selleby, Q. Chen, J. Odqvist and Y. Du, *Crit. Crev. Solid State* **35** (2010) 125-152.
[24] L. Li, W. Yu, Y. Long and C. Jin, *Solid State Comm.* **137** (2006) 358–361.
[25] J.F. Weiher, B.L. Chamberland and J.L. Gillson, *J. Solid State Chem.* **3** (1971) 529–532.
[26] A. Atkinson and R.I. Taylor, *J. Mater. Sci.* **13** (1978) 427-432.
[27] H. Yokokawa, T. Horita, N. Sakai, K. Yamaji, M.E. Brito, Y.-P. Xiong and H. Kishimoto, *Solid State Ionics* **177** (2006) 3193–3198.